Geophysical Journal International

Geophys. J. Int. (2013) **194,** 316–321
Advance Access publication 2013 April 5

doi: 10.1093/gji/ggt094

Constraining the characteristics of tsunami waves from deformable submarine slides

Robert Weiss,[1] Sebastian Krastel,[2] Andreas Anasetti[3] and Kai Wünnemann[4]

[1] *Department of Geosciences, Virginia Tech, Blacksburg, VA, USA. E-mail: weiszr@vt.edu*
[2] *Institute of Geosciences, Christian-Albrechts-Universität, Kiel, Germany*
[3] *GEOMAR; Helmholtz Centre for Ocean Research Kiel, Germany*
[4] *Museum für Naturkunde, Leibniz Institute for Research on Evolution and Biodiversity a the Humboldt University, Berlin, Germany*

Accepted 2013 March 6. Received 2013 March 5; in original form 2012 December 14

SUMMARY

As a marine hazard, submarine slope failures have the potential to directly destroy offshore infrastructure, and, if a tsunami is generated, it also endangers the life of those who live and work at the coastline. The hazard and risk from tsunamis generated by submarine mass failure is difficult to quantify and evaluate due to the problems to constrain the characteristics of the triggered submarine landslide, which introduces unquantifiable uncertainty to hazard assessments based on numerical modelling. To lower the uncertainty, we present a method that determines material parameters for the slide body to constrain the generated tsunami waves. Our method employs the distribution of landslide run-out masses and their comparison with simulations. It assumes that the slide material can be approximated by bulk values during the slide motion. To demonstrate our method, we make use of Valdes slide run-out masses off the Chilean coast.

Key words: Tsunamis.

1 INTRODUCTION

The assessment of submarine slope failure is becoming more important as the number and relevance of offshore structures increase and because coastal metropoles gain power in the light of economic globalization (Masson *et al.* 2006). The potential danger emanates from two agents, of which one is the moving submarine mass itself. After the submarine slope failure, the submarine landslide travels down the submarine slope, which can take place in a violent fashion destroying everything in its path like subaerial landslides and avalanches do. The second agent is due to the fact that submarine landslides displace the water, which can result in the generation of tsunami waves. These tsunami waves, if significant in characteristics, can then destroy offshore, near-shore and onshore infrastructure and endanger the lives of people within the flood zone. As an example of the lethal power of landslide-generated tsunami, there was a loss of more than 2000 people along a 30-km stretch of coastline in Papua New Guinea (PNG) in 1998 when a tsunami wave that had a maximum flow depth of 15 m was generated by a submarine landslide. A M_w 7.1 earthquake triggered this landslide off the PNG coast (Tappin *et al.* 2001; Okal *et al.* 2002).

However, not only earthquakes trigger tsunamigenic submarine landslides; sea level rise, excess pore pressure, weak layers and tectonic oversteeping of the local slope are additional triggers of submarine slope failure (Masson *et al.* 2006). During tsunamigenic earthquakes, a fraction of the released energy deforms the seafloor, which takes place fast so the water column cannot respond quickly enough to maintain or move toward a gravitational equilibrium (Okal & Synolakis 2004). This also delivers the opportunity to constraint the generated tsunami by measuring the waves and earthquake independently. As an example, we refer to Wei *et al.* (2008) who presented results for the 2008 Peruvian tsunami. This procedure is not easily applicable to landslide-generated tsunami. Although tsunami waves generated by a submarine landslide can be measured, direct and independent measurements of the slide characteristics during slide motion in or near-real time has never been done. Because submarine landslides can be triggered by a multitude of different processes that also can work in unison and with the uncertainty in determining the trigger area, it is very unlikely that a direct measurement will ever be done. For the simulation of tsunamis generated by submarine landslides for hazard or risk assessments, this is a dilemma and the uncertainty in the slide behaviour causes the results of most simulation attempts to be highly speculative, even though the wave model itself is state-of-the-art, verified and validated.

We present a method to determine material parameters for the slide body that result in a more realistic model slide-body behaviour and a constraint of the generated tsunami waves. Our method employs a mapped distribution of landslide run-out masses and their comparison with simulated results. If the characteristics of observed run-out masses are reproduced with a certain amount of confidence, then it is assumed that the dynamic behaviour of the slide is

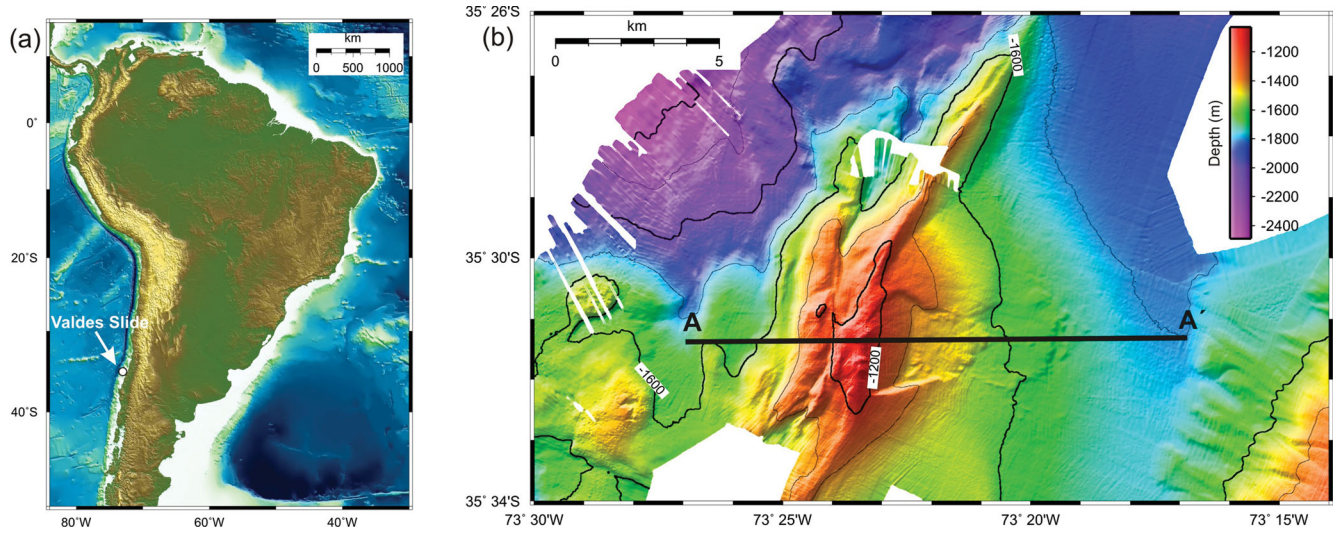

Figure 1. (a) Location of the Valdes slide. (b) High-resolution bathymetry of the slide and location of the cross-section.

sufficiently well represented in the model, and the tsunami waves are constrained. To demonstrate our method, we make use of the Valdes-slide run-out masses off the Chilean coast. Even though our method suffers from the basic assumption that the parameters describing the rheological behaviour of the slide do not change during the slide motion, our method represents a first step toward a better and more constrained understanding of risk and hazard from tsunami waves generated by submarine landslides.

2 THE VALDES SLIDE

The Chilean continental margin is an area of intense tectonic deformation and repeated slope instabilities. More than 60 submarine landslides have been mapped on the continental slope off Southern Chile (32°S–46°S) based on high-resolution bathymetric and seismic reflection data (Völker *et al.* 2012). The Valdes slide is a typical medium-sized slide on the open slope (Fig. 1). It engulfs an area of about ∼23 km^2 and a volume of about ∼0.8 km^3.

In contrast to most other slides along the continental margin, the Valdes Slide is a landward facing slope failure located along the eastern flank of a submarine ridge. The ridge runs SSW–NNE, parallel to subparallel to the continental margin, for ∼80 km at mid-slope level. A recent study (Geersen *et al.* 2011) revealed the relationship between the uplift phase of the ridge with a thrust-fault-system located at greater depths. The uplift of the ridge (up to 600 m above the trench seafloor) created a basin along the middle slope of the continental margin. In case of a thrust fault, the basin generated in the hangingwall above and behind the thrust ridge is termed as piggyback basin. The Valdes slide is situated along the western flank of this piggyback basin at water depths between 1060 and 1800 m. The scar of the slide has an accurate shape with well exposed and steep sidewalls (see Fig. 1b). The run-out of the slide reached 6.2 km. Using a digital elevation model, the morphology of the area before the slide event was reconstructed (Fig. 2) to calculate the volume of the material and understand the possible dynamics of the event. Based on the reconstructed elevation model a total sedimentary volume of about 0.8 km^3 was calculated as missing material from the scar area. The uplift of the ridge, with consequently oversteepening of the seafloor, and the high sedimentation rate of the continental margin are considered the most important pre-conditioning factors of the slide event. The combination of seismic data and core

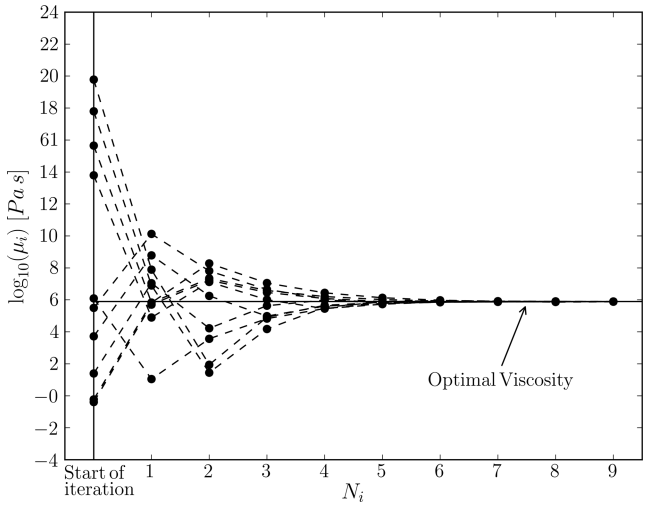

Figure 2. The paths of 10 different simulation to the optimal viscosity for the valdes slide. The initial viscosities were randomly chosen.

analysis suggest that a weak layer acted as sliding surface supporting the slope failure process. The most likely trigger was one of the frequently occurring strong earthquakes in this area.

3 NUMERICAL EXPERIMENTS

3.1 Model description

The computational model that is employed in our study is iSALE,[1] an acronym for Impact Simplified Arbitrary Lagrangian Eulerian hydrocode. iSALE originated from the SALE code that was developed to simulate flows of hydrodynamic materials at all speeds (Amsden *et al.* 1980). However, iSALE only inherited the numerical solver from the original SALE code. iSALE is successfully validated against experimental studies of hypervelocity impacts and also other hydrocodes (Pierazzo *et al.* 2008). With the hydrocode iSALE, the tsunami generation during oceanic meteorite impacts has been explored (e.g. Wünnemann & Lange 2002; Weiss *et al.* 2006; Weiss &

[1] http://www.iSALE-code.de

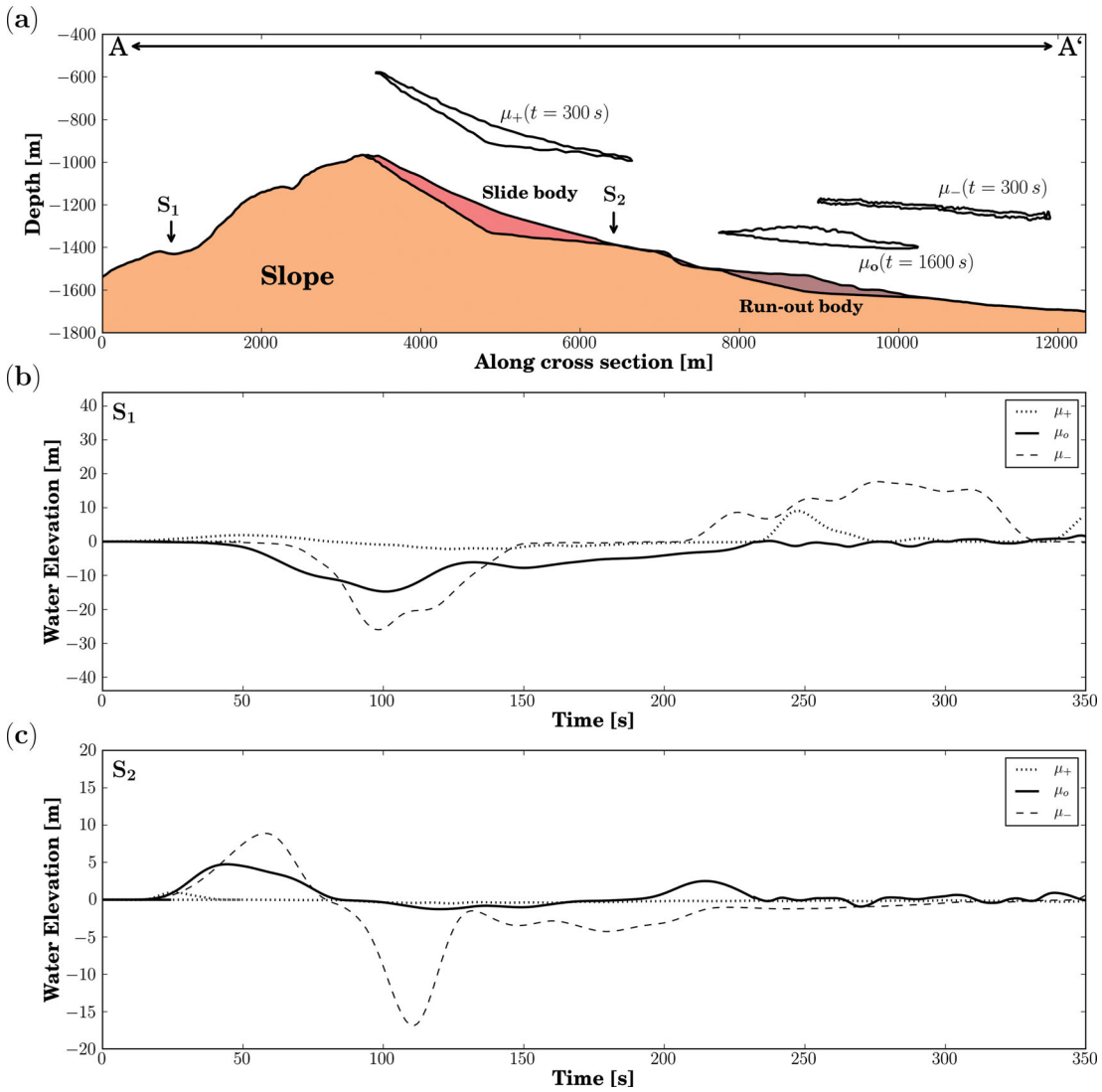

Figure 3. (a) Cross-section from A to A′ from Fig. 1(b) with the initial position of the slide and the location of run-out masses. Also shown are the simulated locations of slide bodies for a viscosity $\mu +$, μ_- and μ_o. Simulated time-series for all three slides in panel (a) are depicted for gauge location S_1 in panel (b) and for S_2 in panel (c).

Wünnemann 2007; Wünnemann *et al.* 2007). Furthermore, iSALE was also used to simulate the generation of tsunami waves during landslides (Weiss *et al.* 2009). For landslide-generated tsunami waves, laboratory experiments of the 1958 Lituya Bay rockslide and tsunami, carried out by Fritz *et al.* (2001), were compared with respective simulations, exhibiting an excellent match of arrival time, amplitude and phase (Weiss *et al.* 2009). The quality of the match provides the confidence that iSALE captures all necessary physics of the non-linear waves generated in the experiments of the 1958 Lituya Bay tsunami and is an appropriate tool for submarine landslide models presented in this study.

The run-out masses of the Valdes slide are distributed predominantly parallel and less normal to the slide motion. To demonstrate that constraints for landslide-generated tsunami waves can be found, for the sake of simplicity and because of the special distribution of the run-out masses, we argue that simulations of the Valdes slide can be carried out on a 2-D mesh with a vertical axis, representing depth, and the horizontal axis-oriented parallel to the sliding direction. The spatial resolution is in both direction constant at $\mathrm{d}x = \mathrm{d}z = 5\,\mathrm{m}$. The bathymetry is chosen along the line A–A′ in Fig. 1(b) and is depicted in Fig. 3(a), in which the red-coloured body represents the slide at time $t = 0$, and the brown-coloured area depicts the location and extend of the run-out masses. In the simulations, the material properties of basalt with a very high Yield strength is employed to prevent deformation and movement of the slope (orange colour). The water is inviscid because viscous effect at the chosen grid scale can be neglected. For simplicity, we assume that the slide body is a Newtonian fluid (constant viscosity). The interface between slope and slide body has the same material properties as the slide body. The viscosity of the slide is also the parameter that will be changed in the course of matching procedure of the simulated with the observed run-out masses.

3.2 Viscosity optimization problem

As described in the previous section, the viscosity of the slide body is the variable that is determined by simulations. It should be noted that a more complex strength model for the slide material, for example Von Mises', Lundborg's or Drucker-Prager's, could been have

been chosen; however, viscosity was taken for the sake of simplicity, only. To find the optimal viscosity for the Valdes slide body, we employ an iterative procedure that is based on bisection and respective constraining conditions. It is unrealistic to fully match the slide geometry in its entire complexity. However, just taking the farthest extend of the run-out masses should already give a good starting point for future methods that are able to take more comprehensive and more complex geometric properties of the run-out masses into account. At the beginning of a simulation, the minimum and maximum viscosity is defined between $\mu_{\min} = 1 \times 10^{-3}$ Pas and $\mu_{\max} = 1 \times 10^{24}$ Pas. Both limiting viscosities were chosen based on the observation that outside this interval, no measurable differences occur in the slide-body dynamics. A starting viscosity is chosen randomly between the minimum and maximum viscosities. iSALE is started, and the motion of the slide body is monitored by detecting the front, back for the slide, and the velocity v_b in the centre of the slide mass. If the slide body does not move or move very slowly ($v_b < 0.2\,\mathrm{m\,s^{-1}}$), the viscosity is two large. The new viscosity (μ_n) is determined by computing the arithmetic average between the starting viscosity and the minimum viscosity. The starting viscosity becomes the maximum viscosity. And iSALE is started again with μ_n. Let us now assume that the slide body travels farther than the maximum extent of the observed run-out masses, then the viscosity is too low. iSALE is again stopped, and viscosity μ_n becomes the minimum viscosity. Then μ_n is computed using the arithmetic mean between $\mu_{\min}$ and $\mu_{\max}$, and iSALE is started with the new viscosity. If the slide body in the simulation reaches within 10 per cent of the maximum extent of the observed run-out masses and the velocity of the slide body is less than $0.2\,\mathrm{m\,s^{-1}}$, iSALE is stopped again, and it is assumed that the optimal viscosity μ_o is found. This procedure is carried out automatically in our computational framework. The geometric and velocity conditions to stop the iteration are defined by balancing the runtime of each individual simulation [$\mathcal{O}$(2–4 weeks)] and how well the simulated run-out masses can reproduce the geometry of the measured deposits, given the grid resolution.

4 RESULTS

4.1 Iteration process

To find the optimal viscosity, μ_o, we employ an iterative procedure, which is, as described earlier, based on interval bisection. We carried out a series of ten runs with randomly chosen initial viscosities within the interval defined by $\mu_{\min}$ and $\mu_{\max}$. Fig. 2 shows the ten runs and how these different runs all converge to the same optimal viscosity. It seems that bisection proves to be a sufficiently effective approach in the simulation framework, because the viscosity converged to the optimal viscosity after only six iterations. The viscosity was within 10 per cent of the optimal viscosity after three iterations for most runs.

Fig. 3(a) depicts positions of the slide bodies for three different initial viscosities from the ensemble shown in Fig. 2. For the slide marked with μ_-, the initial viscosity was $\mu = 5.49 \times 10^1$ Pas. The slide body is shown at $t = 300$ s, and at this time the slide body already travelled beyond the run-out masses observed. The velocity of the centre of mass is still above $15\,\mathrm{m\,s^{-1}}$ at this time, and the slide body disintegrated in a very long and relatively thin geometry. For the slide with μ_+, the initial viscosity is $\mu = 1.32 \times 10^{11}$ Pas. The slide-body geometry did not change much, because the total slide movement was very small, and the velocity of the centre of mass is less than $0.3\,\mathrm{ms^{-1}}$ at $t = 300$ s. The slide marked with μ_o marks the simulation for which the viscosity coincides with the optimal viscosity of $\mu_o = \mu = 7.83 \times 10^5$ Pas. The velocity of the centre of mass was less than $0.15\,\mathrm{m\,s^{-1}}$, and the general shape of the slide is remarkably close to the geometry of the observed run-out masses.

It should be noted that for all three slides, some slide material separated from the main slide body and was deposited on the slope. However, the slide body mass was within 95 per cent of the initial mass for all three scenarios.

4.2 Wave data

The horizontal component of the slide motion generates a wave crest, and the vertical component generates a wave trough. The wave crest travels in the direction of the slide motion. As long as the moving slide body influences the water displacements at the water surface, the wave crest propagates with the speed of the moving slide. After the decoupling, the speed of this wave crest then changes according to the appropriate dispersion relation. The wave trough travels in the direction opposite of the slide motion and is generated during the decoupling of the water cavity that is formed due to the vertical component of the slide motion.

The gauge at position S_1 is located in the opposite direction in which the slide body travels. Therefore, the time-series in Fig. 3(b) exhibit the wave trough arriving first. The amplitude η of the wave trough is about 1 metre for the slide with μ_+, approximately 27 metres for the slide with μ_-, and the amplitude for the slide with μ_o is about 17 metres. The duration of the wave-crest passage varies greatly with 71 s for μ_+, 136 s for μ_-, and 230 s for the slide with μ_o.

As expected, wave crests arrive first at location S_2 in all three time-series (Fig. 3c). The wave crest for the slide with μ_+ is less than a metre in amplitude and is about 10 seconds long. For the slide with μ_-, the amplitude of the crest is about 11 metres with approximately 100 s in duration. For the slide with the optimal viscosity, μ_o, the amplitude of the wave crest is about 5 metres and the duration of the crest is also about 100 s. It can be noted that the time-series for the slide with μ_- also has a wave trough, and the entire wave shape resembles remarkably the *N*-wave as defined in Tadepalli & Synolakis (1996), which are hydrodynamicly stable wave shapes. There is a wave trough behind the crest for slide with the optimal viscosity. The wave trough is less than a metre in amplitude. For μ_- and μ_o, both waves are asymmetrical. However, the wave trough is smaller than the wave crest for μ_-, and for μ_o the wave crest is much larger than the trough.

4.3 Near- and far-field wave evolution

After the generation, the waves propagate away from the source area. During this travel, the waves attenuate due to the geometrical spreading and non-linear processes (energy is shifted from the longer to shorter waves). Without loss of generality, we can assume that the evolution of the wave amplitude is $\eta(r) \propto r^{-q}$, in which r represents the distance to the source area and q is the attenuation exponent. For landslide generated waves, we assume that q varies from 1 to 0.5, where the latter value of the attenuation exponent describes geometrical spreading of shallow-water waves. The attenuation coefficient $q = 1$ was taken from Ward & Asphaug (2000) for non-linear, impact-generated waves, which are thought to be of similar steepness as landslide-generated tsunamis (Wünnemann

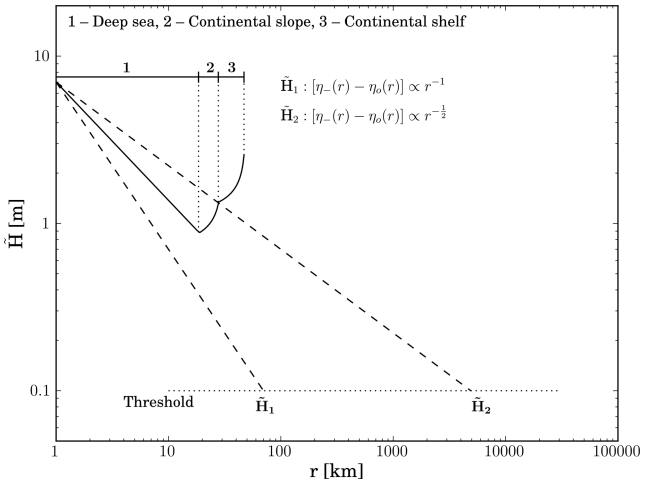

Figure 4. Difference in wave amplitude as a function of distance. The two dashed lines represent two different q in the attenuation relation $\tilde{H}(r) \propto r^{-q}$. The line marked with $\tilde{H}$ represents $q = 1$ and the line marked with $\tilde{H}$ is for $q = 0.5$. The solid line shows the $\tilde{H}$ ($q = 0.7$) for the Valdes slide.

et al. 2010). To study the influence of the initial wave amplitude from the slides with μ_o and μ_-, we define $\tilde{H}$ with $\tilde{H}(r) = \eta_-(r) - \eta_o(r)$ as the difference in the wave amplitude as a function of distance. Fig. 4 shows $\tilde{H}_1$ for $q = 1$, for which a threshold of 0.1 is reached at $r = 75$ km distance from the source are. For $q = 0.5$, the difference $\tilde{H}_1$ drops below the threshold of 0.1 *m* at a distance of $r = 6000$ km.

The Valdes slide is about 200 km west of the Chilean coastline with three major geometric features. For Fig. 4, we defined a constant-depth part (denoted with 1) with a constant depth of 1500 m. The portion denoted with 2 represents the continental slope within which the water depth decreases from 1500 to 200 m. Then the part denoted with 3 is the continental shelf where the water depth further decreases from 200 to 20 m. In the constant-depth part, we assume $q = 0.7$. The changes in water depth over the continental slope and shelf need to be taken into account. The Green's law can be employed to account for wave shoaling. Interestingly, in the original derivation of Green's law, periodic and linear waves were assumed. Even if intuitively Green's law is valid for solitary and other tsunami-like waves, it was not until Synolakis (1991) that intuition was replaced by factual confidence. We employ $\eta(r)/\eta_o = (\mathrm{d}(r)/d_o)^{(1/4)}$, to account for the changing water depth. The parameters η_o and d_o are the initial wave amplitudes and water depth at the slope toe for propagation over the continental slope and the wave amplitude and water depth at shelf break for the propagation over the continental shelf. The final result is that the difference $\tilde{H}$ at the most shoreward is $\tilde{H} = 2.8$ m, which is about 50 per cent of $\tilde{H}$ at 1-km distance from the source area.

5 DISCUSSION AND CONCLUSION

In this contribution, we employed an iterative procedure to match simulated run-out masses with mapped run-out deposits of the Valdes slide off the Chilean coast. As constrain for this procedure, we use the location of the mapped deposits and the velocity of the simulated slide. The parameter that is varied to find a match is viscosity. If the slide body exceeds the mapped deposits and the velocity of the slide when it exceeds the location of the mapped deposits is larger than 0.2 ms^{-1}, it is assumed that the viscosity was too low. On the other hand, if the slide body does not reach the mapped deposits and the velocity of the slide is less than 1 ms^{-1}, the viscosity is too large. For both cases, the velocity will then be adjusted with bisection. We demonstrated in Fig. 2 that for the Valdes slide, there is a unique optimal viscosity, μ_o, even if the initial viscosity is random. Without loss of generality, we assume that this is true for all slides as long as the distribution of the run-out deposits is known.

Furthermore, the time-series at locations S_1 and S_2 suggest that there is no simple relationship between the viscosity of the slide and the characteristics of the generated waves. This leads us to the conclusion that simple and linear scaling laws to quantify the influence of the viscosity, or more general the rheology, of the slide body on the tsunami wave characteristics may not exist. It seems that more parameters need to be taken into account in future simulations. Such parameters may be linked to the properties of the seabed over which the slides masses travel (i.e. bed roughness).

In Fig. 4 we show that the difference in wave amplitude with distance to the source in general, and for the Valdes in particular, is significant. For the Valdes slide, we demonstrate how generated waves can be constrained with mapped slide run-out deposits. This can be generalized to influence hazard assessments for tsunamis from submarine and subaerial landslides. If in a certain area slide run-out masses are mapped, with the described method, the optimal viscosity for the mapped slides can be determined. Once the optimized viscosity is known, it can be assumed that future slides have the same or similar viscosity. With this optimized viscosity, a parameter study with increased robustness and reliability can be carried out to link size and magnitude of the slide to the generated waves, which inevitably results in better tsunami hazard assessments that include submarine and subaerial landslides as tsunami sources.

ACKNOWLEDGEMENTS

RW was supported by the NSF grant ENG-CMMI-0928654. SK expresses his gratitude to Deutsche Forschungsgemeinschaft (DFG, German Science Foundation) for funding this project in the frame of the Cluster of Excellence 'The Future Oceans'.

REFERENCES

Amsden, A., Ruppel, H. & Hirt, C., 1980. Sale: a simplified ale computer program for fluid flows at all speeds. Tech. Rep. LA-8095 Report, Los Alamos National Laboratories.

Fritz, H., Hager, W. & Minor, H.-E., 2001. Lituya bay case: rockslide impact and wave runup, *Sci. Tsunami Hazards,* **19,** 2–22.

Geersen, J., Behrmann, J.H., Völker, D., Krastel, S., Ranero, C.R., Diaz-Naveas, J. & Weinrebe, W., 2011. Active tectonics of the South Chilean marine fore arc, *Tectonics,* **30,** TC3006, doi:10.1029/2010TC002777.

Masson, D., Harbitz, C.B., Wynn, R., Pedersen, G. & Lovholt, F., 2006. Submarine landslides: processes, triggers and hazard prediction. Philosophical Transactions of the Royal Society A: Mathematical, *Phys. Eng. Sci.,* **364,** 2009–2039.

Okal, E., Borrero, J. & Synolakis, C., 2002. Solving the puzzle of the 1998 Papua New Guinea tsunami: the case for a slump, in *Solutions to Coastal Disasters,* pp. 863–877, eds Wallendorf, L. & Ewing, L., Amer. Soc. Civil Eng.

Okal, E. & Synolakis, C., 2004. Source discriminats for near-field tsunamis, *Geophys. J. Int.,* **158**(3), 363–369.

Pierazzo *et al.*, 2008. Validation of numerical codes for impact and explosion cratering, *Meteorit. Planet. Sci.,* **43,** 1917–1938.

Synolakis, C., 1991. Green's law and the evolution of solitary waves, *Phys. Fluids A,* **3,** 190–191.

Tadepalli, S. & Synolakis, C., 1996. Model for the leading waves of tsunamis, *Phys. Rev. Lett.,* **77**(10), 2141–2144.

Tappin, D., Watts, P., McMurty, M., Lafoy, Y. & Matsumoto, T., 2001. The Sissano, Papua New Guinea tsunami of July 1998, *Mar. Geol.,* **175,** 1–23.

Völker, D., Geersen, J., Weinrebe, W. & Behrmann, J., 2012. Submarine mass wasting off Southern Central: distribution and possible mechanisms of slope failure at an active continental margin, in *Submarine Mass Movement and their Consequences: Advances in Natural and Technological Hazards Research,* Vol. 31, pp. 379–390, Springer, Dordrecht.

Ward, S.N. & Asphaug, E., 2000. Asteroid impact tsunami: a probabilistic hazard assessment, *Icarus,* **145,** 64–78.

Wei, Y. *et al.*, 2008. Real-time experimental forecast of the Peruvian tsunami of August 2007 for U.S. coastlines, *Geophys. Res. Lett.,* **35,** L04609, doi:10.1029/2007GL032250.

Weiss, R., Fritz, H. M. & Wünnemann, K., 2009. Hybrid modeling of the mega-tsunami runup in Lituya Bay after half a century, *Geophys. Res. Lett.,* **36,** L09602, doi:10.1029/2009GL037814.

Weiss, R. & Wünnemann, K., 2007. Large waves caused by oceanic impacts of meteorites, in *Tsunami and Non-linear Wave,* pp. 237–261, ed. Kunda, A., Springer, Heidelberg.

Weiss, R., Wünnemann, K. & Bahlburg, H., 2006. Numerical modelling of generation, propagation and run-up of tsunamis caused by oceanic impacts: model strategy and technical solutions, *Geophys. J. Int.,* **167**(1), 77–88.

Wünnemann, K. & Lange, M., 2002. Numerical modeling of impact-induced modifications of the deep-sea floor, *Deep-Sea Research II,* **49,** 669–981.

Wünnemann, K., Weiss, R. & Hofmann, K., 2007. Characteristics of oceanic impact-induced large water waves–re-evaluation of the tsunami hazard, *Meteorit. Planet. Sci.,* **42**(11), 1893–1903.

Wünnemann, K., Collins, G.S. & Weiss, R., 2010. Impact of cosmic bodies into Earth's Oceans and the generation of large tsunami waves: insights from numerical modeling, *Rev. Geophys.,* **48,** RG4006, doi:10.1029/2009RG000308.